Nanoscale Advances

ROYAL SOCIETY OF CHEMISTRY

PAPER

View Article Online
View Journal | View Issue

Cite this: *Nanoscale Adv.*, 2022, **4**, 2501

Rare earth metal (Sm)-doped $NiMnO_3$ nanostructures for highly competent alkaline oxygen evolution reaction

S. Swathi,[a] R. Yuvakkumar,*[a] G. Ravi,[a] Abdullah G. Al-Sehemi[bc] and Dhayalan Velauthapillai*[d]

In the present work, samarium-doped nickel manganese oxide was produced by employing a straightforward co-precipitation method. A peak with a 2θ of 36° corresponded to the (110) plane confirming the formation of the rhombohedral crystal structure of $NiMnO_3$. The existence of Mn–O and Ni–O stretching vibration modes was confirmed by Raman spectroscopy. FTIR spectra confirmed the existence of the metal–oxygen bond of $NiMnO_3$. The synthesized ternary Ni-based material was found to be spherical nanoparticles with an average diameter of 0.81 μm. The electrochemical oxygen evolution reaction (OER) performance was explored on 0.02 M samarium (Sm)-doped $NiMnO_3$ demonstrating outstanding OER action with low 321 mV, a low Tafel slope value (109 mV dec^{-1}), and low charge-transfer resistance (0.19 Ω). Moreover, the BET results suggest that the 0.02 M Sm-doped $NiMnO_3$ exhibited elevated surface area (78.78 m^2 g^{-1}) with a mesoporous character. Therefore, $NiMnO_3$ doped with high concentrations of a rare earth metal, Sm, is proposed as a suitable material for next-generation water splitting applications.

Received 10th January 2022
Accepted 7th April 2022

DOI: 10.1039/d2na00022a

rsc.li/nanoscale-advances

1. Introduction

Water splitting is a spotless and sustainable approach for energy-conversion applications. Interestingly, extensive methods, such as electrochemical, photoelectrochemical, thermal and photocatalytic techniques, *etc.*, have been used for water splitting applications.[1,2] Among the various methods, electrochemical water splitting is a user-friendly technique with unique advantages, such as zero emissions, high energy density and conversion efficiencies, *etc.*[3] The main aim of water splitting techniques is to decrease the overpotential and increase the efficiency of various electrocatalyst materials.[4] Recently, various oxides, sulfides, phosphides, nitrides, alloys, chalcogenides, *etc.* have been employed because of their high catalytic activities and natural abundance.[5]

Transition metal oxides are promising materials for various applications, such as for use in lithium-ion batteries, supercapacitors, water oxidation, hydrogen production, and urea oxidation.[6] However, they have limited application due to their poor conductivity and insufficient active sites. Attempts have been made to overcome these issues by various approaches, such as the incorporation of metal ions, the introduction of carbon-based materials and quantum dots, *etc.*[7] In particular, rare earth metal-doped metal oxides exhibit excellent activities, which improve the conductivity of the material and the surface area, and enhance the diffusion paths.[8] Numerous rare-earth metals, such as gadolinium, neodymium, dysprosium, and samarium have been used as doping agents.[9] Among these metals, samarium dramatically improves the ionic conductivity, carrier transportability, and catalytic performance.[10] In addition, nickel-based materials have gained special attention for the oxygen evolution reactions (OER) due to their benefits of lower water oxidation potential.[11] Many methods are now available to prepare metal oxide electrocatalysts *via* hydrothermal, co-precipitation and microwave-assisted techniques, *etc.*[12] Amongst these, co-precipitation is a less time-consuming technique performed at low temperatures.[13]

Numerous researchers have assessed the application of nickel manganese oxide (NMO) for various purposes. For example, Mustafa Al Samarai *et al.*[14] synthesized a graphene-supported Ni_3MnO_4 catalyst by a reverse micellar method for electrocatalytic OER. Yan Zhang *et al.*[15] synthesized a nickel manganese composite oxide nanomesh *via* the hydrothermal method, followed by high-temperature calcination for use in supercapacitors and electrochemical water oxidation. Dongxiao Ji *et al.*[16] fabricated carbon-based nickel and manganese oxide nanoparticles *via* the electrospinning-calcination method for electrochemical water oxidation. In this study, NMO was

[a]*Department of Physics, Alagappa University, Karaikudi 630 003, Tamil Nadu, India. E-mail: yuvakkumarr@alagappauniversity.ac.in*

[b]*Research Centre for Advanced Materials Science, King Khalid University, Abha 61413, Saudi Arabia*

[c]*Department of Chemistry, King Khalid University, Abha 61413, Saudi Arabia*

[d]*Faculty of Engineering and Science, Western Norway University of Applied Sciences, Bergen 5063, Norway. E-mail: dhayalan.Velauthapillai@hvl.no*

synthesized from the co-precipitation and subsequent calcinations for the OER. Structural and morphological studies confirmed the formation of $NiMnO_3$ nanocomposite. In addition, the doping agent, samarium, not only changed the electrical properties of the nanocomposite but also improved the electrochemical performance of the nanocomposite material.

2. Experimental procedure

Chemical reagents, such as nickel(II) and manganese(II) nitrate [$(Ni(NO_3)_2$, $(Mn(NO_3)_2$], sodium bicarbonate ($NaHCO_3$), ethanol (C_2H_5OH), and methanol (CH_3OH), were procured. NMO was produced by a simple co-precipitation technique. In brief, an equal (1 : 1) molar ratio of nickel and manganese precursors was mixed and dissolved with 50 ml of deionized water. After stirring well, 1.0 M sodium bicarbonate was added; within some hours, a green-bluish precipitate appeared, which was washed with distilled water, ethanol, and methanol. The material thus obtained was transferred to the oven at 80 °C for 12 h. After drying, the product was annealed at 400 °C for 4 h. The formation of a black fine powder indicated the formation of NMO. Likewise, different concentrations of samarium (0.01 and 0.02 M)-doped NMO samples were synthesized by the above procedure using appropriate ratios of materials. The black powder samples were labeled NMO1, NMO2, and NMO3. The electrochemical water oxidation analysis of the synthesized products was examined in three electrode workstations. In these workstations, platinum was used as a counter electrode, Ag/AgCl was used as a reference electrode. The NMO samples were employed as working electrodes with 1 M KOH as the electrolyte.

3. Results and discussion

The XRD spectra were used to examine pure $NiMnO_3$, as well as different concentrations (0.01, 0.02 M) of Sm-doped $NiMnO_3$. The diffraction peaks at 25, 34, 37, 42, 51, 55, 64, and 66° belonged to the (012), (104), (110), (113), (024), (116), (214), and (300) crystal faces of $NiMnO_3$. The XRD indexed peaks were well-oriented with the standard JCPDS (#00-012-0269) with the space group R. The rhombohedral crystal structure of $NiMnO_3$ is shown in Fig. 1A. No other characteristic peaks can be observed in Fig. 1A(b and c), indicating that the doping agent, Sm, did not introduce a second crystal phase in $NiMnO_3$.[17] The average crystalline sizes of the synthesized products, such as NMO1, NMO2, and NMO3, were 35.53, 17.76, and 14.81 nm respectively. Fig. 1B shows Raman spectra for pure $NiMnO_3$ and different concentrations (0.01, 0.02 M) of Sm-doped $NiMnO_3$.

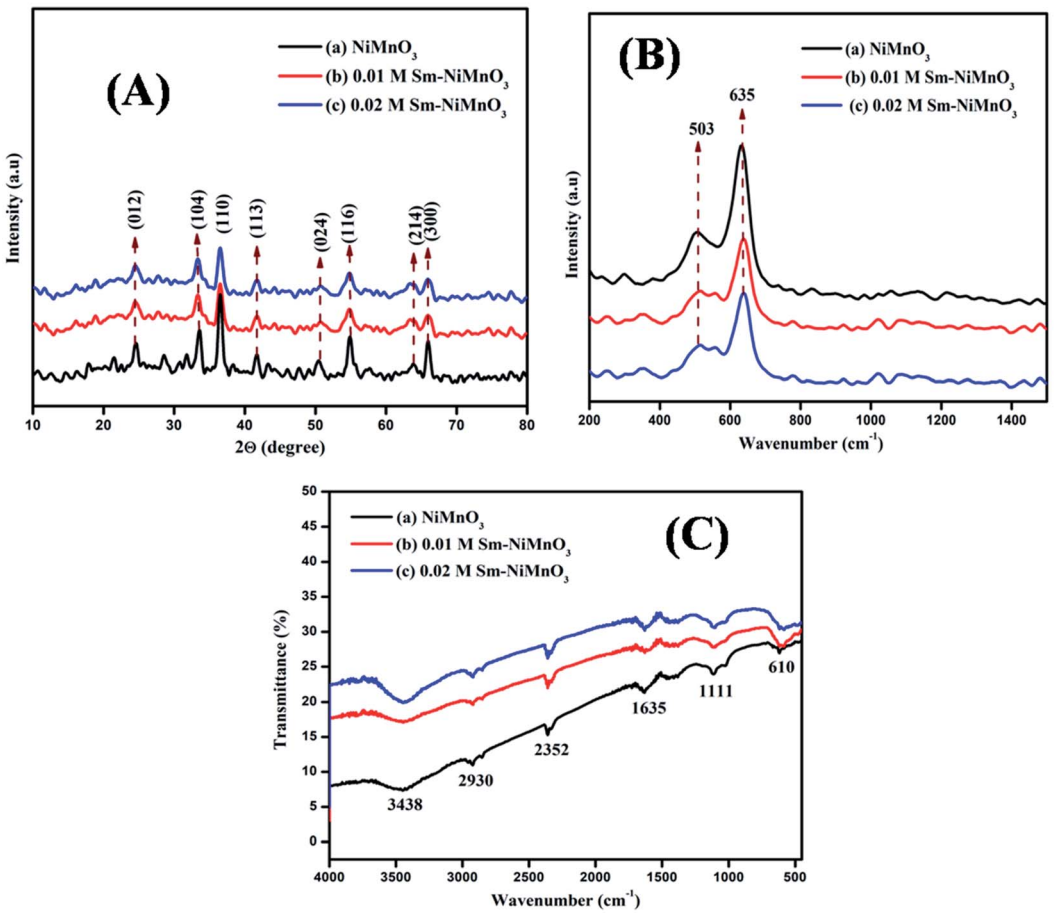

Fig. 1 (A) XRD spectra (B) Raman, and (C) FTIR spectra of pristine $NiMnO_3$, 0.01 M Sm-doped $NiMnO_3$, and 0.02 M Sm-doped $NiMnO_3$.

Two peaks, 503 and 635 cm^{-1}, were observed at the wavenumber range from 200 to 1400 cm^{-1}. The strong band at 635 cm^{-1} revealed asymmetric Mn–O stretching and the weak band located at 503 cm^{-1} indicated Ni–O stretching.[18] Fig. 1C shows the FTIR spectra of pure $NiMnO_3$ and different concentrations (0.01, 0.02 M) of Sm-doped $NiMnO_3$ structures. The absorption bands at 3438 and 1635 cm^{-1} revealed H–O–H water vibrations. The absorption bands present below 1111 cm^{-1} corresponded to $NiMnO_3$; the band at 610 cm^{-1} revealed a metal–oxygen $NiMnO_3$ bond. The bands observed at 2930 and 2352 cm^{-1} were ascribed to C–H bonds.[19]

Fig. 2(A–F) shows the SEM images of pure $NiMnO_3$ and different concentrations (0.01, 0.02 M) of Sm-doped $NiMnO_3$, suggesting the particles to be in the micro range in size between 10 and 5 μm. The images revealed that the particles have a spherical shape with diameters of 2.26 μm (pure $NiMnO_3$), 2.0 μm (0.01 M Sm-doped $NiMnO_3$), and 0.81 μm (0.02 M Sm-doped $NiMnO_3$). These sizes were calculated using the Image J software. In a zoomed-in view, fine nanoparticles were seen to coexist (Fig. 2B, D and F). Moreover, it was observable that the particle size of $NiMnO_3$ decreased from 2.26 to 0.81 μm, when the content of Sm dopant increased from 0 to 0.02 M. The agglomeration was also slightly reduced because of doping. In addition, the average particle sizes may decrease with increasing Sm concentrations, due to the existence of smaller radii. In detail, the ionic radius of Sm^{3+} was 1.08 Å and Ni^{3+} was

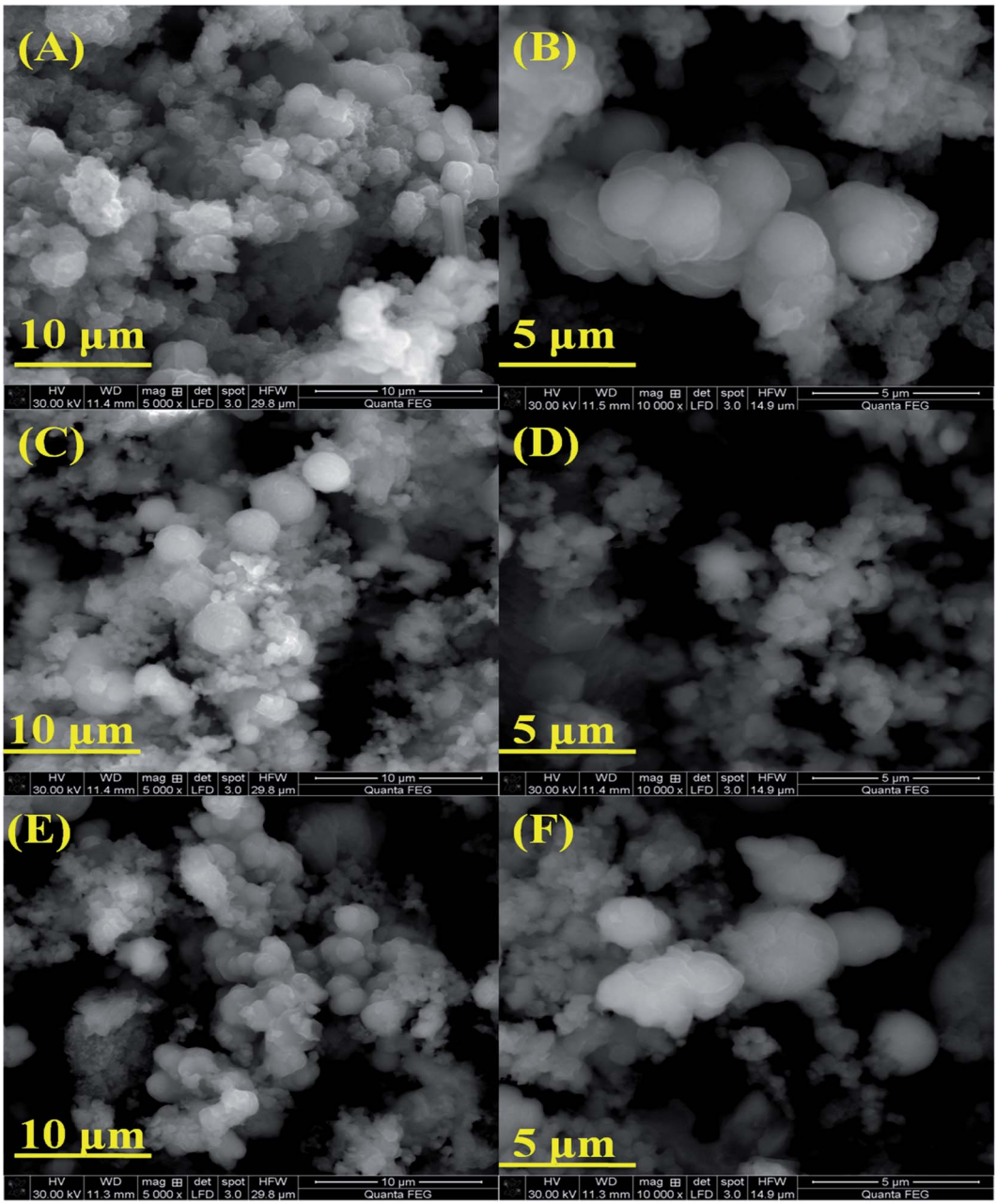

Fig. 2 SEM images (A and B) pristine $NiMnO_3$, (C and D) 0.01 M Sm-doped $NiMnO_3$, and (E and F) 0.02 M Sm-doped $NiMnO_3$ at 10 and 5 μm.

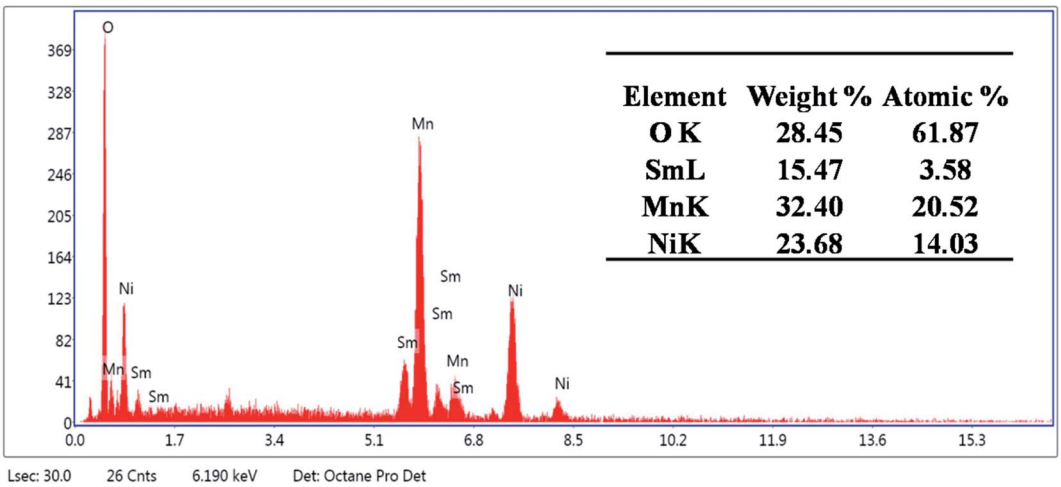

Fig. 3 An EDX spectra of 0.02 M Sm-doped $NiMnO_3$.

70 Å. Therefore, the radius of Sm^{3+} was very small as compared to that of Ni^{3+}. Furthermore, smaller average particle sizes may be attributed due to inhibited grain growth due to the substituted Sm ions at the Ni sites. The reduced particle sizes significantly promoted the edge and corner-site contact at the catalyst surface, which enabled the formation of reaction intermediates, accelerated catalytic kinetics, and enhanced electrochemical water oxidation.[20,21] Overall, SEM analysis suggested that increased dopant concentrations decreased the particle size, denoting that the synthesized product developed a more crystalline nature.[22]

The incorporation of the doping agent, Sm, was confirmed by the EDX spectra as shown in Fig. 3. The synthesized material comprised 23.68% Ni, 32.40% Mn, 28.45% O, and 15.47% Sm by weight percentage. Moreover, the sample contained 14.03% Ni, 20.52% Mn, 61.87% O, and 3.58% Sm by atomic percentage. No other elements representing impurities were observed.

Fig. 4 shows the results of the BET surface area analysis of pure, 0.01 M, and 0.02 M Sm-doped $NiMnO_3$. According to the BET studies, the surface area, pore-volume, and diameter of pure, 0.01 M, and 0.02 M Sm-doped $NiMnO_3$ were found and are presented in Table 1. Results revealed that 0.02 M Sm-doped $NiMnO_3$ had a higher surface area than other materials. Moreover, the obtained graphs depict a type IV isotherm with discrete H4 hysteresis, proving the mesoporous nature of the synthesized material. The high surface area and porous properties of the 0.02 M Sm-doped $NiMnO_3$ can reduce diffusion lengths, facilitating the penetration of electrolyte ions and improving the transport pathway in the electrochemical analysis.[23] Moreover, the elevated surface area offers additional

Table 1 BET analysis of the prepared materials

Materials	Surface area	Pore volume	Pore diameter
$NiMnO_3$	38.065 $m^2\ g^{-1}$	0.174 cc g^{-1}	1.960 nm
0.01 M Sm–$NiMnO_3$	44.332 $m^2\ g^{-1}$	0.176 cc g^{-1}	14.857 nm
0.02 M Sm–$NiMnO_3$	78.78 $m^2\ g^{-1}$	0.439 cc g^{-1}	11.252 nm

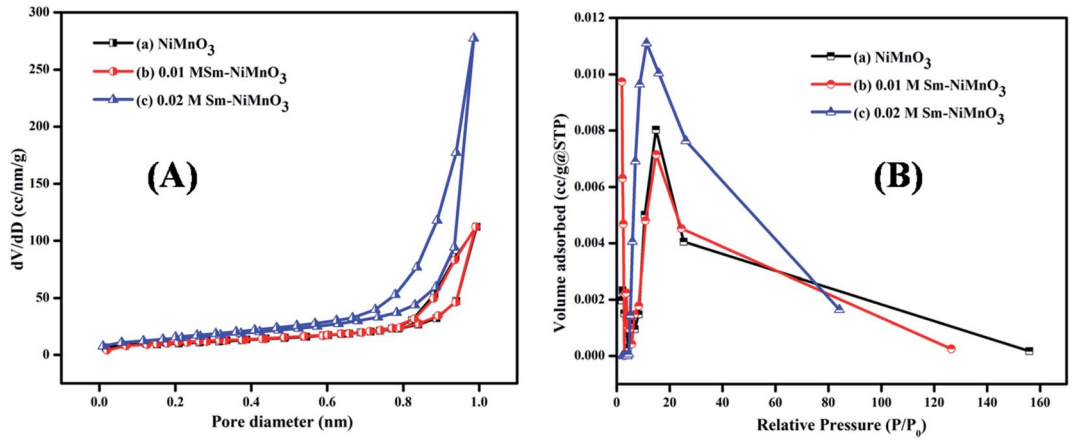

Fig. 4 (A) Nitrogen adsorption–desorption and (B) BJH pore diameter of pristine $NiMnO_3$, 0.01 M Sm-doped $NiMnO_3$, and 0.02 M Sm-doped $NiMnO_3$.

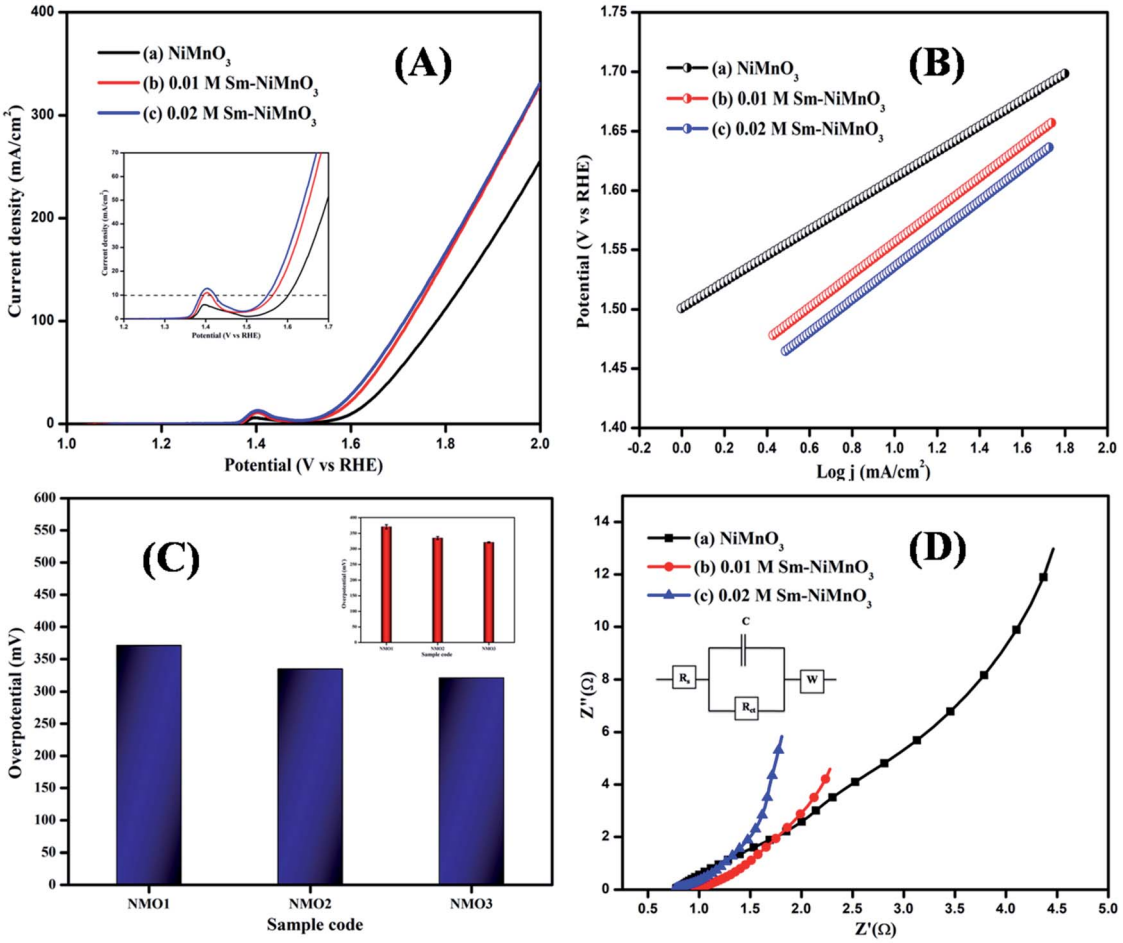

Fig. 5 (A) LSV spectra, (B) Tafel slope (C) Bar diagram (inset: error bar), and (D) EIS spectra of pristine $NiMnO_3$, 0.01 M Sm-doped $NiMnO_3$, and 0.02 M Sm-doped $NiMnO_3$.

active sites and helps improve electrochemical OER performance.

The LSV curves of pure, 0.01 M, and 0.02 M Sm-doped $NiMnO_3$ were recorded from 0 to 1 V at 2 mV s^{-1} (Fig. 5A). The 0.02 M Sm-doped $NiMnO_3$ showed better OER activity and required only 321 mV to reach the benchmark of 10 mA cm^{-2}. Contrarily, the other electrocatalysts, such as pristine $NiMnO_3$ and 0.01 M Sm-doped $NiMnO_3$, need 371 and 335 mV to attain the same current density (Fig. 5C). Generally, Ni-based binary or ternary materials exhibit excellent electrochemical performance than pure Ni materials.[24] Moreover, the rare earth dopant, Sm, also improved the surface area, further improving the OER activity. The electrode material had a larger surface area as compared to the electrocatalyst. Hence, superior electrochemical performance was expected due to the addition of Sm to $NiMnO_3$, which could, in turn, produce high electrochemical OER activity. A comparison of these findings with those from previous literature is tabulated in Table 2.

Table 2 A comparison of results obtained here with that of previous works

Material	Overpotential values	Tafel slope values	Ref.
NiO	396 mV	54 mV dec^{-1}	25
$NiFe_2O_4$ hollow fiber/Ni foam	433 mV	134 mV dec^{-1}	26
3D NiO_x/Ni foam	390 mV	80 mV dec^{-1}	27
NiO hollow nanofibers/Ni foam	340 mV	84 mV dec^{-1}	28
$Ni_{0.9}Fe_{0.1}O_x$	340 mV	31 mV dec^{-1}	29
MnO_2 NSs	423 mV	79.6 mV dec^{-1}	30
MnO_2 NSs/Co_3O_4 NPs-1:2	355 mV	56.5 mV dec^{-1}	30
Sm-$NiMnO_3$	321 mV	109 mV dec^{-1}	[Present work]

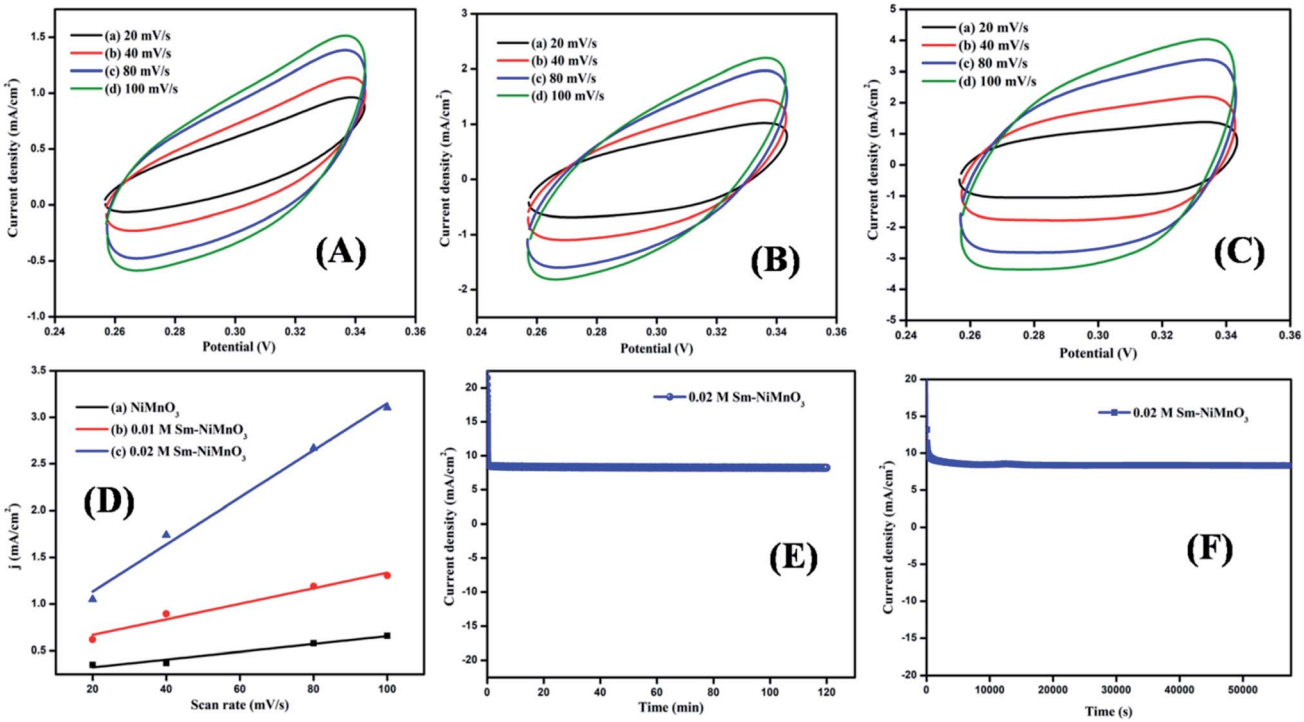

Fig. 6 (A–C) CV Curves and (D) double-layer capacitance for pristine $NiMnO_3$, 0.01 M, 0.02 M Sm-doped $NiMnO_3$, chronoamperometry test of 0.02 M Sm-doped $NiMnO_3$ for (E) 2 h and (F) 16 h.

Tafel slope curves were derived from the polarization curves, which were then used to investigate the material OER kinetics (Fig. 5B). Tafel slopes of 138, 136, and 109 mV/dec were obtained for pure $NiMnO_3$, 0.01 M, and 0.02 M Sm-doped $NiMnO_3$. 0.02 M Sm-doped $NiMnO_3$ showed a small slope of 109 mV/dec as compared to the other two materials. A low Tafel slope value denotes rapid electron transport and superb OER catalytic kinetics.[31]

The EIS analysis was performed on all prepared materials, to obtain further information on OER kinetics (Fig. 5D). 0.02 M Sm-doped $NiMnO_3$ presented charge transfer (R_{ct}) and solution resistance (R_s) of 0.19 and 0.76 Ω, respectively, which were smaller than those of other materials, *i.e.*, 0.01 M Sm doped $NiMnO_3$ (R_s = 0.77 Ω, R_{ct} = 0.20 Ω) and pure $NiMnO_3$ (R_s = 0.96 Ω, R_{ct} = 0.26 Ω). The fitted equivalent circuit has been inserted in Fig. 5D. These results suggest that the 0.02 M Sm-doped $NiMnO_3$ had more favorable OER kinetics because a low R_{ct} value denotes highly proficient charge transfer and a speedier faradaic process.[32]

The electrochemical activity towards OER was further studied with the help of double-layer capacitance. The cyclic voltammogram was obtained at a potential of 0.26–0.34 V at various scan rates of 20, 40, 80, and 100 mV s^{-1}, respectively (Fig. 6(A–C)). As predicted, 0.02 M Sm-doped $NiMnO_3$ showed C_{dl} values of 25.2 mF cm^{-2}, whereas the 0.01 M Sm-doped $NiMnO_3$ and pure $NiMnO_3$ showed the C_{dl} values of 8.3 and 4.1 mF cm^{-2}, respectively (Fig. 5D). Moreover, the electrochemical active surface area (ECSA) was estimated following the equation: ECSA = C_{dl}/C_s; C_{dl} - double-layer capacitance and C_s - sample-specific capacitance. The estimated ECSA of pure $NiMnO_3$, 0.01 M, and 0.02 M-Sm doped $NiMnO_3$ were 0.205, 0.415, and 1.26 cm^2 respectively. These results suggest that the incorporation of Sm in $NiMnO_3$ provided greater surface area, which could offer additional exposed surface reactive sites for OER activity.[33]

A durability test for 0.02 M Sm-doped $NiMnO_3$ was performed using chronoamperometry (Fig. 6E and F). No further changes were observed in the current density of 0.02 M Sm-doped $NiMnO_3$ with 98.5% retention after 2 h (Fig. 6E). Moreover, the same electrode was tested again for 16 h, whereby it exhibited 97.6% retention, clearly suggesting the material's stability in prolonged hours (Fig. 6F). Overall, the results suggest that the introduction of Sm to $NiMnO_3$ imparts excellent OER activity and stability to $NiMnO_3$ owing to the higher surface area, electrical conductivity, and abundance of catalytic active sites in the Sm-doped material.[34]

4. Conclusion

Different concentrations of pure and Sm-doped $NiMnO_3$ were synthesized by employing a low-temperature co-precipitation technique. The structures and shapes of the electrocatalysts thus produced were determined by XRD, Raman, FTIR, and SEM analyses. In addition, the existence of Sm was confirmed using EDX analysis to confirm that no other trace elements existed in the synthesized sample. Electrochemical studies showed that 0.02 M Sm-doped $NiMnO_3$ exhibited a high double-layer capacitance (C_{dl}) of 25.2 mF cm^{-2} and a high

electrochemically active surface area of 1.26 cm^2. In addition, the 0.02 M Sm-doped $NiMnO_3$ exhibited excellent stability and OER performance at 321 mV as compared to other samples, such as pure $NiMnO_3$ (371 mV) and 0.01 M Sm-doped $NiMnO_3$ (335 mV). Therefore, the incorporation of the rare earth element, samarium (Sm), improved the surface area, charge-transfer ability, and efficacy of the catalytic active sites.

Conflicts of interest

There are no conflicts to declare.

Acknowledgements

This work was supported by MHRD RUSA–Phase 2, UGC-SAP, DST-FIST, and PURSE grants. Thanks to Open Access Funding (OA-fond) (oa-fond@hvl.no) at Western Norway University of Applied Sciences, Norway. The authors are thankful for the support provided by the Research Center for Advanced Materials Science at King Khalid University, Saudi Arabia for funding this work under grant no: RCAMS/KKU/p002-21.

References

1 H. Sun, X. Xu, Y. Song, W. Zhou and Z. Shao, Designing High-Valence Metal Sites for Electrochemical Water Splitting, *Adv. Funct. Mater.*, 2021, **31**(16), 2009779.
2 Y. Wang, G. Qian, Q. Xu, H. Zhang, F. Shen, L. Luo and S. Yin, Industrially promising IrNi-FeNi3 hybrid nanosheets for overall water splitting catalysis at large current density, *Appl. Catal., B*, 2021, **286**, 119881.
3 Q. Sun, Y. Tong, P. Chen, B. Zhou and X. Dong, Universal Strategy of Bimetal Heterostructures as Superior Bifunctional Catalysts for Electrochemical Water Splitting, *ACS Sustainable Chem. Eng.*, 2021, **9**(11), 4206–4212.
4 W. Li, C. Wang and X. Lu, Integrated transition metal and compounds with carbon nanomaterials for electrochemical water splitting, *J. Mater. Chem. A*, 2021, **9**(7), 3786–3827.
5 S. Li, E. Li, X. An, X. Hao, Z. Jiang and G. Guan, Transition-metal-based catalysts for electrochemical water splitting at high current density: current status and perspectives, *Nanoscale*, 2021, **13**, 12788–12817.
6 D. Jiang, S. Xu, M. Gao, Y. Lu, Y. Liu, S. Sun and D. Li, Synergistically Integrating Nickel Porous Nanosheets with 5d Transition Metal Oxides Enabling Efficient Electrocatalytic Overall Water Splitting, *Inorg. Chem.*, 2021, **60**(11), 8189–8199.
7 Y. Zhang, J. Yang, Z. Yu, Y. Hou, R. Jiang, J. Huang, F. Yang, S. Yao, L. Gao and W. Tang, Modulating carbon-supported transition metal oxide by electron-giving and electron-absorbing functional groups towards efficient overall water splitting, *Chem. Eng. J.*, 2021, **416**, 129124.
8 J. D. Rodney, S. Deepapriya, M. C. Robinson, C. J. Raj, S. Perumal, B. C. Kim, S. Krishnan and S. J. Das, Dysprosium doped copper oxide (Cu1–*x*Dy*x*O) nanoparticles enabled bifunctional electrode for overall water splitting, *Int. J. Hydrogen Energy*, 2021, **46**(54), 27585–27596.
9 M. Rong, H. Zhong, S. Wang, X. Ma and Z. Cao, La/Ce doped CoFe Layered double hydroxides (LDH) highly enhanced oxygen evolution performance of water splitting, *Colloids Surf. A: Physicochem. Eng. Asp.*, 2021, 126896.
10 A. K. Vishwakarma, M. Hussain, S. K. Verma, V. Shukla, M. A. Shaz and O. N. Srivastava, Synthesis and characterizations of graphene/Sm doped $BiFeO_3$ composites photoanode for efficient photo-electrochemical water splitting, *Int. J. Hydrogen Energy*, 2021, **46**(29), 15550–15560.
11 P. M. Bodhankar, P. B. Sarawade, G. Singh, A. Vinu and D. S. Dhawale, Recent advances in highly active nanostructured NiFe LDH catalyst for electrochemical water splitting, *J. Mater. Chem. A*, 2021, **9**(6), 3180–3208.
12 T. Carbonati, C. Cionti, E. Cosaert, B. Nimmegeers, D. Meroni and D. Poelman, NIR emitting GdVO4: Nd nanoparticles for bioimaging: The role of the synthetic pathway, *J. Alloys Compd.*, 2021, **862**, 158413.
13 S. V. M. Goorabjavari, F. Golmohamadi, S. Haririmonfared, H. Ahmadi, S. Golisani, H. Yari, A. Hasan, Z. Edis, M. Ale-Ebrahim, M. Sharifi and B. Rasti, Thermodynamic and anticancer properties of inorganic zinc oxide nanoparticles synthesized through co-precipitation method, *J. Mol. Liq.*, 2021, **330**, 115602.
14 M. Al Samarai, A. W. Hahn, A. Beheshti Askari, Y. T. Cui, K. Yamazoe, J. Miyawaki, Y. Harada, O. Rüdiger and S. DeBeer, Elucidation Of Structure–Activity Correlations In A Nickel Manganese Oxide Oxygen Evolution Reaction Catalyst By Operando Ni L-Edge X-Ray Absorption Spectroscopy And 2P3d Resonant Inelastic X-Ray Scattering, *ACS Appl. Mater. Interfaces*, 2019, **11**(42), 38595–38605.
15 Y. Zhang, H. Zhang, L. Fang, J. Deng and Y. Wang, Facile synthesis of nickel manganese composite oxide nanomesh for efficient oxygen evolution reaction and supercapacitors, *Electrochim. Acta*, 2017, **245**, 32–40.
16 D. Ji, J. Sun, L. Tian, A. Chinnappan, T. Zhang, W. A. D. M. Jayathilaka, R. Gosh, C. Baskar, Q. Zhang and S. Ramakrishna, Engineering of the heterointerface of porous carbon nanofiber–supported nickel and manganese oxide nanoparticle for highly efficient bifunctional oxygen catalysis, *Adv. Funct. Mater.*, 2020, **30**(13), 1910568.
17 X. Xie, T. Otremba, P. Littlewood, R. Schomäcker and A. Thomas, One-pot synthesis of supported, nanocrystalline nickel manganese oxide for dry reforming of methane, *ACS Catal.*, 2013, **3**(2), 224–229.
18 Y. L. Ding, B. M. Goh, H. Zhang, K. P. Loh and L. Lu, Single-crystalline nanotubes of spinel lithium nickel manganese oxide with lithium titanate anode for high-rate lithium ion batteries, *J. Power Sources*, 2013, **236**, 1–9.
19 S. Periyasamy, P. Subramanian, E. Levi, D. Aurbach, A. Gedanken and A. Schechter, Exceptionally active and stable spinel nickel manganese oxide electrocatalysts for urea oxidation reaction, *ACS Appl. Mater. Interfaces*, 2016, **8**(19), 12176–12185.

20 G. S. Lotey and N. K. Verma, Structural, magnetic, and electrical properties of Gd-doped $BiFeO_3$ nanoparticles with reduced particle size, *J. Nanopart. Res.*, 2012, **14**(3), 1–11.

21 K. Fominykh, P. Chernev, I. Zaharieva, J. Sicklinger, G. Stefanic, M. Döblinger, A. Müller, A. Pokharel, S. Böcklein, C. Scheu and T. Bein, Iron-doped nickel oxide nanocrystals as highly efficient electrocatalysts for alkaline water splitting, *ACS Nano*, 2015, **9**(5), 5180–5188.

22 T. Nguyen, S. Eugénio, M. Boudard, L. Rapenne, M. J. Carmezim, T. M. Silva and M. F. Montemor, Hybrid nickel manganese oxide nanosheet–3D metallic dendrite percolation network electrodes for high-rate electrochemical energy storage, *Nanoscale*, 2015, **7**(29), 12452–12459.

23 C. H. Wu, J. S. Ma and C. H. Lu, Synthesis and characterization of nickel–manganese oxide *via* the hydrothermal route for electrochemical capacitors, *Curr. Appl. Phys.*, 2012, **12**(4), 1190–1194.

24 P. T. Babar, A. C. Lokhande, M. G. Gang, B. S. Pawar, S. M. Pawar and J. H. Kim, Thermally oxidized porous NiO as an efficient oxygen evolution reaction (OER) electrocatalyst for electrochemical water splitting application, *J. Ind. Eng. Chem.*, 2018, **60**, 493–497.

25 R. Liu, F. Liang, W. Zhou, Y. Yang and Z. Zhu, Calcium-doped lanthanum nickelate layered perovskite and nickel oxide nano-hybrid for highly efficient water oxidation, *Nano Energy*, 2015, **12**, 115–122.

26 V. D. Silva, L. S. Ferreira, T. A. Simões, E. S. Medeiros and D. A. Macedo, 1D hollow MFe_2O_4 (M= Cu, Co, Ni) fibers by Solution Blow Spinning for oxygen evolution reaction, *J. Colloid Interface Sci.*, 2019, **540**, 59–65.

27 G. Q. Han, Y. R. Liu, W. H. Hu, B. Dong, X. Li, X. Shang, Y. M. Chai, Y. Q. Liu and C. G. Liu, Three dimensional nickel oxides/nickel structure by *in situ* electro-oxidation of nickel foam as robust electrocatalyst for oxygen evolution reaction, *Appl. Surf. Sci.*, 2015, **359**, 172–176.

28 V. D. Silva, T. A. Simoes, F. J. Loureiro, D. P. Fagg, F. M. Figueiredo, E. S. Medeiros and D. A. Macedo, Solution blow spun nickel oxide/carbon nanocomposite hollow fibres as an efficient oxygen evolution reaction electrocatalyst, *Int. J. Hydrogen Energy*, 2019, **44**(29), 14877–14888.

29 L. Trotochaud, J. K. Ranney, K. N. Williams and S. W. Boettcher, Solution-cast metal oxide thin film electrocatalysts for oxygen evolution, *J. Am. Chem. Soc.*, 2012, **134**(41), 17253–17261.

30 C. Wang, F. Wang, S. Y. Qiu, J. Gao, L. L. Gu, K. X. Wang, P. J. Zuo, K. N. Sun and X. D. Zhu, Integrating Co_3O_4 nanoparticles with MnO_2 nanosheets as bifunctional electrocatalysts for water splitting, *Int. J. Hydrogen Energy*, 2021, **46**(17), 10356–10365.

31 S. A. Khan, S. B. Khan and A. M. Asiri, Electro-catalyst based on cerium doped cobalt oxide for oxygen evolution reaction in electrochemical water splitting, *J. Mater. Sci.: Mater. Electron.*, 2016, **27**(5), 5294–5302.

32 K. Xu, Z. Zhu, W. Guo, H. Zhang, T. Yu, W. Wei, W. Liang, D. Zhang, M. He and T. Yang, Cerium oxide modified iridium nanorods for highly efficient electrochemical water splitting, *Chem. Commun.*, 2021, **57**(70), 8798–8801.

33 D. Gao, R. Liu, J. Biskupek, U. Kaiser, Y. F. Song and C. Streb, Modular Design of Noble-Metal-Free Mixed Metal Oxide Electrocatalysts for Complete Water Splitting, *Angew. Chem., Int. Ed.*, 2019, **58**(14), 4644–4648.

34 H. Wang, H. W. Lee, Y. Deng, Z. Lu, P. C. Hsu, Y. Liu, D. Lin and Y. Cui, Bifunctional non-noble metal oxide nanoparticle electrocatalysts through lithium-induced conversion for overall water splitting, *Nat. Commun.*, 2015, **6**(1), 1–8.